

Design optimization of a structurally flexible wave energy converter

Austin S. Berrier and Bryony L. DuPont

Abstract—Several wave energy converter (WEC) design archetypes have been recently proposed that are made of flexible materials. These designs use electroactive materials to directly incorporate their power take off (PTO) units into their hull, and are capable of extracting power by damping structural deformations. The built-in system redundancy of flexible WECs is designed to reduce the cost of a single PTO failure as well as decrease system deployment complexity. Due to the small number of developers and researchers working with flexible WECs, however, the design space of flexible WECs is still largely unexplored in practice, and no work to date has used an optimization algorithm to tune the geometric parameters of a flexible WEC design to its deployment location. Here we study increasing the mean power output of a flexible submerged tube by first co-optimizing its geometry and submergence, and next optimizing its material parameters. We use a deterministic discrete pattern search algorithm to aim for a pragmatically low number of function evaluations to convergence, and model each potential device using customized degrees of freedom in the boundary element method software Capytaine. We determine that tuning the geometry of a device to its deployment location can lead to significant improvements in power output from a reference design, while tuning the material parameters only leads to marginal improvements. We anticipate that our work can be used as a case study for using optimization algorithms to improve the performance of other flexible WEC design archetypes.

Index Terms—Design optimization, Flexible materials, Structural analysis, Generalized body modes

I. INTRODUCTION

COMMERCIAL wave energy projects to date are primarily design archetypes that generate power from rigid body motion. These designs typically resonate at a single incident wave frequency, and typically require control strategies to increase the frequency range of power capture. Control strategies are used to effectively force system resonance, and come at the cost of additional system complexity and potentially high motion amplitudes or PTO component forces in PTO

The ID number of this paper submission is 2094 submitted to track WDD.

Authors are affiliated with the Pacific Marine Energy Center. A.S. Berrier is a graduate student in Mechanical Engineering at Oregon State University 2000 SW Monroe Ave, Corvallis, OR 97331 U.S.A (e-mail: berriera@oregonstate.edu).

B.L. DuPont is an Assistant Professor in Mechanical Engineering at Oregon State University 2000 SW Monroe Ave, Corvallis, OR 97331 U.S.A (e-mail: Bryony.DuPont@oregonstate.edu).

This research was supported by an appointment with Marine and Hydrokinetic Graduate Student Research Program sponsored by the U.S. Department of Energy (DOE), Office of Energy Efficiency and Renewable Energy, and Water Power Technologies Office. This program is administered by the Oak Ridge Institute for Science and Education (ORISE) for the DOE. ORISE is managed by ORAU under DOE contract number DESC0014664. All opinions expressed in this paper are the author's and do not necessarily reflect the policies and views of DOE, ORAU, or ORISE.

components, requiring extensive repairs. To address the inherent limitations of a single degree of freedom system, some wave energy developers and researchers have proposed flexible WEC design archetypes that are able to resonate at any number of incident wave frequencies. Flexible WEC designs could be potentially unrolled at their deployment instead of being directly towed, simplifying construction logistics and complexity.

Flexible design archetypes include variants of their rigid body counterparts, including oscillating surge devices [1], attenuators [2], heaving point absorbers [3], and oscillating water columns [4]. Another notable device includes the Anaconda, which uses traveling deformation waves to harness power at its end [5]. We study here the flexible equivalent of a rigid body attenuator design, a submerged flexible tube similar to that being developed by SBM Offshore, Inc., and built out of a dielectric elastomer generator material [6]. The material itself combined with power electronics can be used to convert power directly from wave induced mechanical deformations [7]. Flexible devices are modeled as continuous systems, and have an infinite number of resonant frequencies. Because of this, we can tune the resonant frequencies of the tube to respond the most to the incident wave environment.

A few wave energy devices have been made or studied that are made of flexible materials. Much work has gone into just studying the capabilities of these devices without regards to control strategies. Most work to date uses an objective function of produced power or produced power divided out by a cost proxy of surface area or volume.

WEC hydrodynamic research to date has primarily focused on rigid body systems, and design optimization of WEC designs have too to improve device objectives such as power performance, leveled cost of energy proxies, economic return, or component reliability. Much is then left unexplored in using optimization algorithms to improve optimal designs for flexible wave energy. We explore here optimizing the design of a flexible WEC in two stages - first, co-optimizing its geometry and submergence; and second, optimizing the material parameters of a reference design.

II. DESIGN ASSESSMENT

Wave energy converter design optimization is typically performed using a set of geometry parameters to assess a device. The algorithm used to optimize a device can be pragmatically based on the required time to evaluate each design's objective, as well as the number of design variables and search space complexity.

For example, [8] and [9] both studied optimizing the radii and drafts of a two-body heaving cylinder model, while both [10] and [11] used a genetic algorithm to improve the hydrodynamic design of a device using bicubic surfaces.

We outline here the automated process used to assess each set of flexible tube design variables \vec{x} . This design was first modeled by [12] and further studied by [13], and we build entirely off their modeling work here. The geometry of each tube can be completely described by its static radius r_s and length L . Its spatial location is described by its submergence z_s and pitch angle θ_p if we locate it at 0 degrees relative to incident waves, although we consider only a horizontally oriented tube here ($\theta_p = 0$).

We quantify each design performance by its expected annual power output at Humboldt Bay, California. Each function evaluation time takes an extensive amount of time (5 minutes up to 1 hour), so we prioritize obtaining an improved design in as few iterations as possible. We do this by making discrete search step sizes \vec{d} in the design space \vec{x} that get progressively smaller over each optimization run. In this way, we can obtain an improved solution in less than approximately 50 total iterations.

A. Design Variables

We sequentially performed two different optimization setups as two different ways to approach optimizing a flexible WEC design:

- 1) Tube geometry and submergence, given fixed material parameters:

$$\vec{x} = [r, L, z_s]$$

- a) r_s , the static radius of the tube
- b) L , the length of the tube
- c) z_s , the average submergence of the tube

Where $K_{mat} = 900 \text{ kPa/m}^2$ and $T_s = 38 \text{ kN}$ and are described next.

- 2) Tube material properties, given a fixed design geometry and submergence:

$$\vec{x} = [K_{mat}, T_s]$$

- a) K_{mat} , the stiffness of the elastic material
- b) T_s , the pretension in the material fibers

Where r_s , L , and z_s correspond to the starting reference design used in 1).

Each search variables was bounded and discretized with the values in the following table:

Variable \in [Bounds]	Discretization
$r_s \in [0.1, 2.5] \text{ m}$	0.1
$L \in [20, 200] \text{ m}$	2.5
$z_s \in [-25.0, -0.1] \text{ m}$	0.25
$K_{mat} \in [100, 3000] \text{ kPa/m}^2$	50
$T_s \in [10, 200] \text{ kN}$	2

B. Constants

Values listed in the following table are constant for each tube design for all design optimizations.

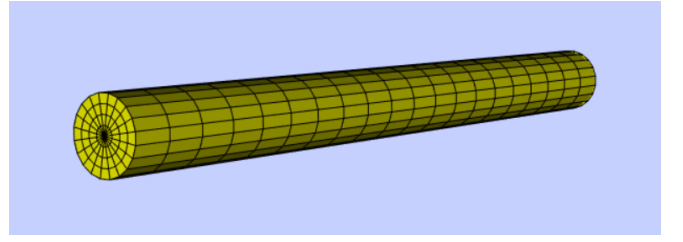


Fig. 1. Example mesh of submerged tube

Variable	Name	Value
Mode count	N	5
Tube thickness	t	0.10 m
Tube density	ρ_{tube}	532.6 kg/m ³
Tube material damping	B_{mat}	17.8 kPa·s
Viscous damping coefficient	B_R	$8\pi \cdot 10^{-6}$
Water density	ρ	1000 kg/m ³
Water depth	d	$-\infty \text{ m}$

C. Meshing

Each design mesh is generated as a cylindrical tube with its center at $(0, 0, z_s)$. The shortest deep water incident wavelength at our deployment location is 16.4 m, so using the meshing suggestions given by [14], we use a characteristic length along the tube's length of 1.0 m. An example mesh is shown in Fig. 1.

D. Creating Mode Shapes

To assess the modal vibrations of the bulging device, we can define N custom degrees of freedom in a frequency domain boundary element method tool that correspond to the device's deformation modes. This is known as generalized body modes analysis, and has been used to study structural deflections in both rigid body and flexible devices. We follow here the mathematical procedure of [12], who derived the modal equations of motion for the device, and the notation and modal matrices of [13].

We first define the modal variable $\chi(x, t)$ such that $\partial\chi/\partial t = U(x, t)$, the velocity of the fluid inside of the enclosed tube.

Using mass conservation and the assumption of small radial deformation amplitudes, we can use a Taylor series approximation to define the axisymmetric radial deformation δr of any point along the tube due to each mode:

$$\begin{aligned} \delta r &= r(x, t) - r_s \\ \delta r &= r_s \sqrt{1 - \frac{\partial\chi}{\partial x}} - r_s \\ \delta r &\approx -\frac{r_s}{2} \frac{\partial\chi}{\partial x} \end{aligned}$$

To define $\chi(x, t)$ for each set of design variables, we first need to solve the nonlinear dispersion relationship

for modal frequency ω_n

$$\begin{aligned} 0 &= \frac{k_{n,1}L}{2} \tanh\left(\frac{K_{n,1}}{2}\right) - \frac{K_{n,1}L}{2} \tan\left(\frac{k_{n,1}L}{2}\right) \\ 0 &= \frac{K_{n,2}L}{2} \tanh\left(\frac{K_{n,2}}{2}\right) - \frac{k_{n,2}L}{2} \tan\left(\frac{k_{n,2}L}{2}\right) \\ &\quad - \frac{\rho\pi r_s^2 L \cdot \omega_{n,2}^2}{-M\omega_{n,2}^2 + 2K_m} \left(\frac{K_{n,2}}{k_{n,2}} + \frac{k_{n,2}}{K_{n,2}}\right) \\ &\quad \cdot \tanh\left(\frac{K_{n,1}}{2}\right) \tan\left(\frac{k_{n,2}L}{2}\right) \end{aligned}$$

Where the modal wavenumbers $k_{n,i}$ and $K_{n,i}$ for each of the two mode types ($i = 1, 2$) are related to each set of frequency roots $\omega_{n,1}$ and $\omega_{n,2}$:

$$\begin{aligned} k_{n,i}^2 &= \frac{2\pi}{DT_s} \left(\sqrt{1 + \frac{1}{\pi} T_s \rho D^2 \cdot \omega_{n,i}^2} - 1 \right) \\ K_{n,i}^2 &= \frac{2\pi}{DT_s} \left(\sqrt{1 + \frac{1}{\pi} T_s \rho D^2 \cdot \omega_{n,i}^2} + 1 \right) \end{aligned}$$

Each set of nonlinear equations is solved by first discretizing a set of modal frequencies from a small value ϵ to 2π rad/s. Each root was found by checking where a small change in frequency caused a change in sign of $g(\omega)$ or $h(\omega)$. Each of these frequencies was then used as a starting point for SciPy's [15] `fsolve` function to numerically find each actual root ω_k . The frequencies were then sorted by magnitude from smallest to largest, and then trimmed off after n degrees of freedom. The two different mode shapes are then as follows:

$$\chi_{n,1} = c_1 \sin(k_{n,1}x) - c_2 \sinh(K_{n,1}x) \quad (1)$$

$$\chi_{n,2} = c_3 \cos(k_{n,2}x) + c_4 \cosh(K_{n,2}x) \quad (2)$$

Where the constants c_1 to c_4 are as follows:

$$\begin{aligned} c_1 &= \tanh\left(\frac{K_{n,1}L}{2}\right) / \cos\left(\frac{k_{n,1}L}{2}\right) \\ c_2 &= \tan\left(\frac{k_{n,1}L}{2}\right) / \cosh\left(\frac{K_{n,1}L}{2}\right) \\ c_3 &= K_{n,2} \tanh\left(\frac{K_{n,2}L}{2}\right) / \cos\left(\frac{k_{n,2}L}{2}\right) \\ c_4 &= k_{n,2} \tan\left(\frac{k_{n,2}L}{2}\right) / \cosh\left(\frac{K_{n,2}L}{2}\right) \end{aligned}$$

We then can normalize each function χ_i according to [13]:

$$N_i^2 = \frac{1}{L} \int_{-L/2}^{L/2} \chi_i^2 dx + \frac{M}{\rho\pi r_s^2 L} \left(\chi_i \Big|_{L/2} \right)^2$$

That is, each function χ_i and derivative are redefined as follows:

$$\begin{aligned} \chi_i &:= \frac{1}{N_i} \chi_i \\ \frac{\partial \chi_i}{\partial x} &:= \frac{1}{N_i} \frac{\partial \chi_i}{\partial x} \end{aligned}$$

We then define the radial deformation function δr for each modal frequency, and include them as generalized degrees of freedom in Capytaine. Using the notation of [16], each mesh face centered at location

(x_m, y_m, z_m) will have corresponding Cartesian deformations (u, v, w) :

$$\begin{aligned} u &= 0 \\ v &= \frac{y_m}{r_s} \cdot \delta r \\ w &= \frac{z_m - z_s}{r_s} \cdot \delta r \end{aligned}$$

E. Assessing Modal Response Amplitudes

We then evaluate the added mass $\mathbf{A}(\omega)$, radiation damping $\mathbf{B}_{rad}(\omega)$, and excitation force $\hat{\mathbf{F}}_{ex}(\omega)$ matrices due to the waves radiated by each degree of freedom and diffracted by the still tube in a 0 degree incident wave. The notation $f(\omega)$ here denotes a function f of incident wave frequency ω . All hydrodynamic parameters were found in the boundary element method software Capytaine [17], a Python rewrite of the Matlab code Nemoh [18].

The frequency domain equation of motion for each modal degree of freedom k is as follows:

$$(-\omega^2(\mathbf{M} + \mathbf{A}(\omega)) + i\omega(\mathbf{B}_{rad} + \mathbf{B}(\omega)) + \mathbf{C}) \begin{pmatrix} \hat{a}_1 \\ \vdots \\ \hat{a}_n \end{pmatrix} = \hat{\mathbf{F}}_{ex}(\omega) \quad (3)$$

Where \mathbf{M} , \mathbf{B} , and \mathbf{C} are the frequency independent contributions to the modal mass, damping, and stiffness matrices, respectively evaluated as:

$$\begin{aligned} \mathbf{M} &= \rho\pi r_s^2 L \cdot \mathbf{I}_n \\ \mathbf{B} &= \rho\pi r_s^2 \eta \boldsymbol{\xi} + \rho B_R \boldsymbol{\epsilon} \\ \mathbf{C} &= \begin{bmatrix} \omega_1^2 & & \\ & \ddots & \\ & & \omega_n^2 \end{bmatrix} \mathbf{M} \end{aligned}$$

The modal damping terms $\boldsymbol{\xi}$ and $\boldsymbol{\epsilon}$ are due to wall damping and damping due to the tube's inner flow:

$$\begin{aligned} \xi_{ij} &= \int_{-L/2}^{L/2} \frac{\partial \chi_i}{\partial x} \frac{\partial \chi_j}{\partial x} dx \\ \epsilon_{ij} &= \int_{-L/2}^{L/2} \chi_i \chi_j dx \end{aligned}$$

And the constant η is a dissipation coefficient proportional to the material's total material and power take off damping:

$$\eta = \frac{h_s \pi r_s}{\rho} (B_{mat} + B_{PTO}) \quad (4)$$

Note that ξ_{ij} has the following alternative form that relates to the linearized tube deformations δr :

$$\begin{aligned} \xi_{ij} &= \frac{4}{r_s^2} \int_{-L/2}^{L/2} \left(-\frac{r_s}{2} \frac{\partial \chi_i}{\partial x} \right) \left(-\frac{r_s}{2} \frac{\partial \chi_j}{\partial x} \right) dx \\ \xi_{ij} &= \frac{4}{r_s^2} \int_{-L/2}^{L/2} \delta r_i \delta r_j dx \end{aligned}$$

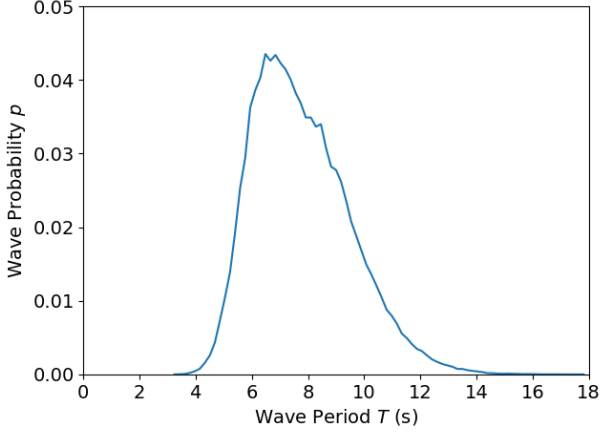


Fig. 2. Probability distribution of incident wave periods at Humboldt Bay, California

We then calculate the total dissipated power spectrum $P_{total}(\omega)$ due to each modal response amplitude velocity $\omega \hat{a}_k$:

$$P_{total}(\omega) = \frac{1}{2} \rho \pi r_s^2 \eta \omega^2 \sum_m^n \sum_l^n \Re(\hat{a}_m \hat{a}_l^*) \xi_{ml} \quad (5)$$

This power spectrum is a useful metric for using the device as a passive or active floating breakwater. We are only interested in the mechanical power dissipated by the PTO $P_{PTO}(\omega)$ damping for potential conversion into electrical power, so we take a ratio of the PTO damping to the total material damping:

$$P_{PTO}(\omega) = \frac{B_{PTO}}{B_{PTO} + B_{mat}} P_{total}(\omega) \quad (6)$$

F. Calculating the Optimization Objective Function

We then use a probability distribution of our potential deployment location's annual wave period distribution to calculate the device's average power output μ_P :

$$\mu_P = \int_0^\infty P_{PTO}(\omega) \cdot p(\omega) d\omega \quad (7)$$

We chose to study an optimal design located at Humboldt Bay, CA, with an annual average wave period spectrum divided into 82 equal period bins [19] $p(\omega)$ shown in Fig. 2:

The device power was found in every regular sea state at this location using a wave height of 1.0 m, similarly to the methodology presented in [20]. We first considered a constrained problem that the tube remain completely submerged in its mean position, so the final objective function was:

$$\begin{aligned} &\text{minimize} && f_{obj} = -\mu_P \\ &\text{subject to} && z_s \leq -r_s \end{aligned}$$

Next, we remove the constraint that the tube remain entirely submerged. Because part of the tube may lie above the free surface, we assume that only the submerged circumference is able to deflect due to incoming waves. We then multiply the final mean dissipated

power value by the proportion of tube circumference C_s below the free surface.

$$\text{minimize } f_{obj} = -C_s \mu_P$$

Where the multiplying constant C_s is given by the continuous function:

$$C_s(z_s) = \begin{cases} 1 & z_s \leq -r_s \\ \frac{\pi - 2 \arcsin(z_s/r_s)}{2\pi} & -r_s < z_s < r_s \\ 0 & z_s \geq r_s \end{cases}$$

A plot of C_s follows in Fig. 3.

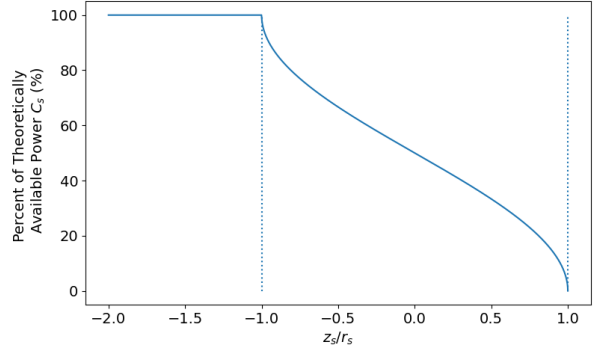


Fig. 3. A percentage of available power for the submerged device as a ratio of its submergence z_s to static radius r_s . The left and right dotted lines respectively correspond to entirely submerged and floating tube designs.

G. Finding the Optimal PTO Damping

After evaluating the hydrodynamic coefficients for a design, we optimize the value B_{PTO} using a one dimensional line search. The hydrodynamic properties of each mesh and modal degrees of freedom are both independent of the PTO damping, so the damping value can be tuned to each design to optimize the tube's total dissipated power. We do this by iteratively solving Equations (3)-(7) for each tested value B_{PTO} , and searching for the maximum value of μ_P . An example of this process is shown in Fig. 6, where we can see that the relationship between B_{PTO} and μ_P has a single maximum value. We can see that the power curve has one peak at the optimal damping value, so a line search method is appropriate.

H. Update design

We then update the current design variables depending on how well it evaluated relative to the last tested design. The entire function evaluation and design variable update process is listed in 1, and can be seen as an extension of a generalized pattern search algorithm without the use of dynamic ordering [21].

III. RESULTS

A. Constrained Geometry Optimization

We use the tube geometry and approximate submergence of the design presented in [13] as a starting point \vec{x}_0 for the algorithm, with design variables as follows:

$$\begin{aligned} \vec{x}_0 &= [r, L, z_s] \\ \vec{x}_0 &= [0.9, 60, -1.25] \text{ m} \end{aligned}$$

Algorithm 1: Discrete optimization algorithm for finding an optimal flexible tube design

Input : Starting design variables \vec{x}_0 , list of possible moves in search space \vec{d} , upper and lower variable bounds, and a starting step size $\alpha = 16$

- 1 . **Output:** Optimal design variables \vec{x}_{opt} and objective function f_{opt} .
- 1) Set the current design location \vec{x}_c and objective function value f_c . This is equal to the starting design variables for the 1st iteration, and the best design found at any time during the optimization run.
 - 2) Attempt a new move in design space $\vec{x}_{new} = \vec{x}_c + \alpha\vec{d}$ along the current search direction.
 - 3) Check that the given design is within the given problem bounds and satisfies the constraint (if applied), and reject the move if not.
 - 4) Generate a mesh using the geometry design variables r_s , L , and z_s .
 - 5) Calculate the design's modal frequencies ω_n using all of the design variables.
 - 6) Create radial deformation modes using the modal frequencies, then convert each mode to Cartesian coordinates for each mesh face.
 - 7) Evaluate the added mass, radiation damping, and excitation force matrices over each incident wave frequency.
 - 8) Repeat steps a) to c) to optimize the damping value B_{PTO} for the design using a line search method.
 - a) Calculate the response amplitude \hat{a}_n for each mode.
 - b) Calculate the dissipated power spectrum $P_{tot}(\omega)$.
 - c) Weight the power spectrum according to the wave environment to find the mean power value μ_P .
 - 9) Find the next search direction to move, and check for convergence.
 - a) If $f_{new} < f_c$, keep the move to the new design \vec{x}_{new} , and keep α at the same value. Set $f_{opt} = f_{new}$, and go to 1).
 - b) If the move is worse, multiply α by -1 to search in the other direction. If both search directions have been checked, go to the next move \vec{d} in the list and go to 2).
 - c) If all variables have been searched without finding any better solution, reduce α by a factor of 1/2 and go to the first search direction \vec{d} . Go to 2).
 - d) If $\alpha = 1$ and there are no better moves along any search direction for any variable, the optimization is considered to be converged. Return \vec{x}_{opt} and f_{opt} .
-

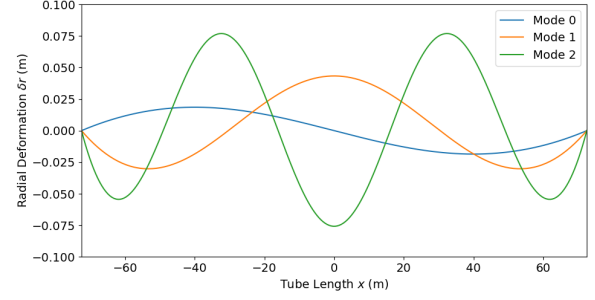


Fig. 4. Radial deformation mode shapes of the optimal constrained design.

For the constrained problem, the algorithm converged to the final design in 24 iterations:

$$[r, L, z_s]_{opt} = [1.1, 145.0, -1.25] \text{ m}$$

The optimal design had a 4.4 times increase in power while requiring an increase in PTO material usage of 3.0 times, leading to a power per material usage increase of 49%. The optimal design is very close to the constraint $z_s \leq -r_s$ but still could be closer given a possible discrete move along either z_s or r_s . We note that the reference design \vec{x}_0 we used was itself close to the imposed constraint, however, and many large discrete moves at the beginning of the optimization were unable to be made because they would violate the constraint (i.e. the tube radius would grow too large or the submergence would be too small).

While the constraint itself was useful for reducing the number of required evaluations to convergence, it does so at the cost of potentially converging to a sub-optimal solution. This could be potentially addressed by adding a fourth discrete move that moves in both the radius and submergence directions, but was not within the scope of this study.

An incident wavelength the length of the optimal 145.0 m tube corresponds to a deep water wave period of 9.64 s, which corresponds to near the deployment location's dominant wave period.

The first three mode shapes of this design can be seen in Fig. 4. Each mode shape has a maximum normalized radial deformation of about 0.10 m, or about 9% of the tube's radius. Multiplying the mode shape by its corresponding response amplitude \hat{a} lets us find the actual deformation along the tube at any given point and incident wave frequency.

The response amplitude operators \hat{a} for the first three modes can be seen in Fig. 5. We can see that the maximum response amplitude decreases for the higher frequency modes that have higher amplitudes, meaning that each of the three shown modes has approximately the same radial deformation as the others at their maximum response. The 0th mode appears to have the largest bandwidth overall, with the 1st and 2nd modes both having a sharper peak along the incident wave periods.

The dissipated power take off power spectrum $P_{PTO}(\omega)$ for the optimal constrained design can be seen in Fig. 6. The period weighted area under this

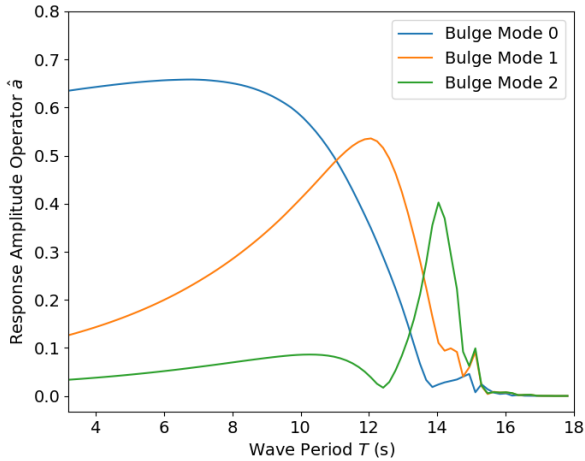


Fig. 5. Response amplitude operators for the five mode shapes of the optimal constrained design.

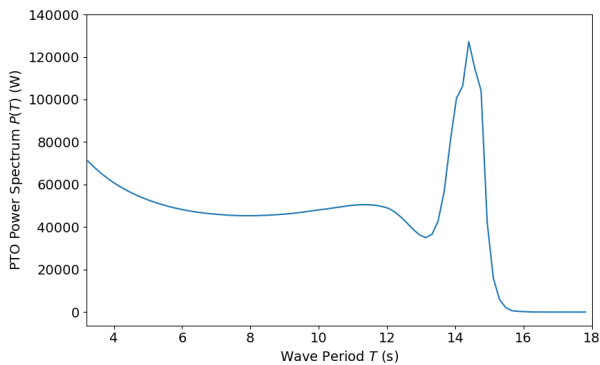


Fig. 6. The dissipated power spectrum of the constrained optimal device

curve gives us the mean dissipated power dissipated by the power take off material μ_P . We see for the optimal constrained design that it has an almost uniform power spectrum for the smallest wave period all the way to 12 second waves. Because 98.2% of all available waves are 12 seconds or less at our simulated deployment location, almost all of the produced power comes from this section. The 2nd mode response peak around 13 to 15 second waves causes a sharp peak in the power spectrum, but this peak is only available to less than 2% of incident waves and so does not contribute a significant amount to the total estimated power.

The optimal power take off damping value for the optimal constrained design can be seen in Fig. 7

B. Material Optimization

The reference design used for the optimization study was for the design variables listed in the geometry study with material values found in [12] and [13].

$$\begin{aligned}\vec{x}_0 &= [K_{mat}, T_s] \\ \vec{x}_0 &= [900, 38] \text{ kPa/m}^2, \text{ kN}\end{aligned}$$

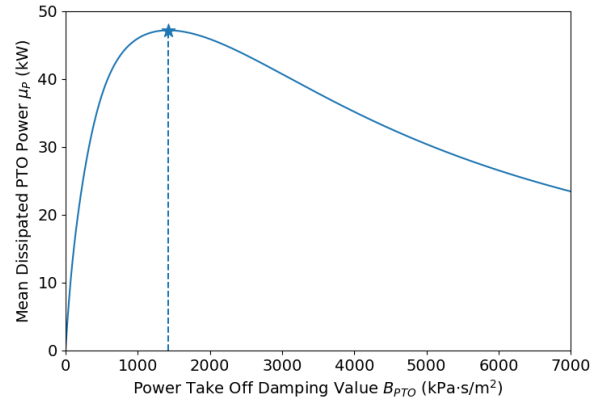


Fig. 7. The relationship between the constant Power Take Off dissipation value and the mean dissipated power by the tube. The single optimal value of B_{PTO} is shown with the dotted line and star.

The unconstrained problem converged to the final design variables in 18 iterations:

$$[K_{mat}, T_s]_{opt} = [100, 200] \text{ kPa/m}^2, \text{ kN}$$

The optimal material parameters point to reducing the stiffness of the rubber material while increasing the pretension in its inlaid fibers as much as possible. We note here that both material parameters are along their respective bounds, but only lead to a marginal improvement in power value (0.44%). Due to the magnitude of this small improvement, we chose not to further study tuning material parameters.

C. Unconstrained Geometry Optimization

The best solution found by removing the submergence constraint was found after 32 iterations and had the following design variables:

$$[r, L, z_s]_{opt} = [2.5, 145.0, -2.75] \text{ m}$$

This design has the same length to the optimal design found using the constraint. The optimization algorithm appears to be favoring finding a larger bounded static radius r_s at that length, and a submergence that places it entirely below the free surface at a submergence to radius ratio of 1.1. This submergence ratio is similar to the design found in the constrained case as well, which had a submergence ratio of 1.14.

Similarly to the constrained case, the improved design has a greater power per surface area ratio than the reference design. The optimal design overall had a 19.6 times increase in mean dissipated power while requiring an increase in PTO material usage of 6.7 times, leading to a power per material usage increase of about 190%. Although this is a promising result, a larger design with a constant thickness would necessarily require more power take off damping to dissipate more power, potentially requiring more system complexity or up-front costs.

IV. CONCLUSIONS

We optimized the design of a submerged flexible wave energy converter by first co-optimizing its submergence and shape, and then optimizing its material parameters. We aimed to improve the expected power output of the device, and found that improvements in the power to surface area of a design could be improved from a given reference design by up to 44%. Increasing the expected power output of a design only lead to minimal improvements, however.

Further work is needed here to directly incorporate a cost proxy to penalize increasing material or power take off design requirements, or by constraining the maximum radial deformation response. More work could be done to study and optimize other flexible design archetypes that have different mode shapes to the submerged tube considered here.

Future work for optimizing a flexible device could be also done using a more accurate model representation of incident wave heights due in an irregular sea state, and may lead to different optimal designs than those presented here. The long function evaluation times required to simulate a single design in this study are an especially interesting use of design optimization algorithms, and more work is needed to determine tradeoffs between design improvements and the computational effort needed to find them.

APPENDIX A CONVERGENCE STUDIES

We ran a convergence study to determine how many modes would be required to adequately describe a defined design's capable mean power take off dissipation. To do this, we increased the number of used simulated modes for our reference design and studied how much additional power each mode contributed to the total. As seen in Fig. 8, we found that only 3 modes were needed to capture 90% of the device's total capable power, and 5 modes were needed to capture approximately 95%. Because of this, we set the number of simulated modes N to be 5 for all other tested designs.

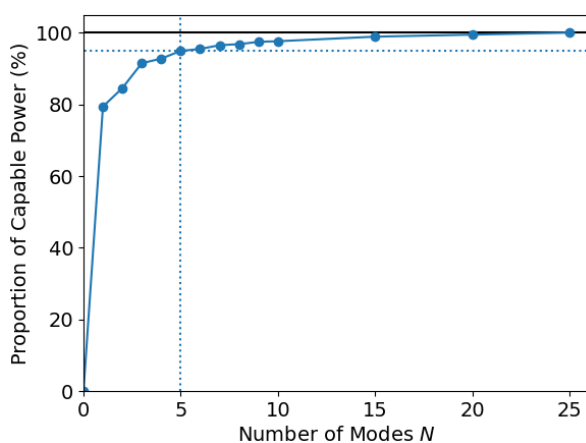


Fig. 8. Mode number convergence study for total dissipated power. The horizontal dotted line shows 95% power using 5 modes, and the solid line shows the 100% total power value using 25 modes.

ACKNOWLEDGEMENT

A.S. Berrier would like to thank Dr. Jennifer van Rij for providing helpful starting code, comments, and hydrodynamic simulation files, and Dr. Yi-Hsiang Yu and Dr. Michael Lawson for help with project planning.

REFERENCES

- [1] B. C. Boren and J. Weber, "Flexible wave energy converter," U.S. Patent 0 054 820, Feb. 2021.
- [2] J. Pollack and P. F. Jean, "Wave energy converter," U.S. Patent 0 019 498, Jan. 2010.
- [3] A. Kurniawan, J. R. Chaplin, D. M. Greaves, and M. Hann, "Wave energy absorption by a floating air bag," *Journal of Fluid Mechanics*, vol. 812, p. 294–320, 2017.
- [4] G. Moretti, G. P. Rosati Papini, L. Daniele, D. Forehand, D. Ingram, R. Vertechy, and M. Fontana, "Modelling and testing of a wave energy converter based on dielectric elastomer generators," *Proceedings of the Royal Society of London Series A*, vol. 475, no. 2222, p. 20180566, Feb. 2019.
- [5] J. R. Chaplin, V. Heller, F. J. M. Farley, G. E. Hearn, and R. C. T. Rainey, "Laboratory testing of the Anaconda," *Philosophical Transactions of the Royal Society A: Mathematical, Physical and Engineering Sciences*, vol. 370, no. 1959, pp. 403–424, Jan. 2012.
- [6] P. Jean, A. Wattez, G. Ardoise, C. Melis, R. Van Kessel, A. Fourmon, E. Barrabino, J. Heemskerck, and J. P. Queau, "Standing wave tube electro active polymer wave energy converter," in *Electroactive Polymer Actuators and Devices (EAPAD) 2012*, ser. Society of Photo-Optical Instrumentation Engineers (SPIE) Conference Series, Y. Bar-Cohen, Ed., vol. 8340, Apr. 2012, p. 83400C.
- [7] C. Graf, J. Maas, and D. Schapeler, "Energy harvesting cycles based on electro active polymers," in *SPIE Smart Structures and Materials + Nondestructive Evaluation and Health Monitoring*, Y. Bar-Cohen, Ed., San Diego, California, USA, Mar. 2010, p. 764217.
- [8] M. Blanco, M. Lafoz, D. Ramirez, G. Navarro, J. Torres, and L. Garcia-Tabares, "Dimensioning of Point Absorbers for Wave Energy Conversion by Means of Differential Evolutionary Algorithms," *IEEE Transactions on Sustainable Energy*, vol. 10, no. 3, pp. 1076–1085, Jul. 2019.
- [9] H. Mankle, Z. Morrell, I. Williams, G. Bacelli, V. Neary, B. DuPont, and R. G. Coe, "Co-optimization of Sizing and Controls for a Point-Absorber Wave Energy Converter," p. 23.
- [10] A. McCabe, "Constrained optimization of the shape of a wave energy collector by genetic algorithm," *Renewable Energy*, vol. 51, pp. 274–284, Mar. 2013.
- [11] A. Garcia-Teruel and D. I. M. Forehand, "Optimal wave energy converter geometry for different modes of motion," p. 8.
- [12] A. Babarit, J. Singh, C. Mélis, A. Wattez, and P. Jean, "A linear numerical model for analysing the hydroelastic response of a flexible electroactive wave energy converter," *Journal of Fluids and Structures*, vol. 74, pp. 356–384, 2017.
- [13] M. Ancellin, M. Dong, P. Jean, and F. Dias, "Far-field maximal power absorption of a bulging cylindrical wave energy converter," *Energies*, vol. 13, no. 20, 2020. [Online]. Available: <https://www.mdpi.com/1996-1073/13/20/5499>
- [14] O. Faltinsen, "Sea loads on ships and offshore structures." [Online]. Available: <https://www.osti.gov/biblio/5464335>
- [15] P. Virtanen, R. Gommers, T. E. Oliphant, M. Haberland, T. Reddy, D. Cournapeau, E. Burovski, P. Peterson, W. Weckesser, J. Bright, S. J. van der Walt, M. Brett, J. Wilson, K. J. Millman, N. Mayorov, A. R. J. Nelson, E. Jones, R. Kern, E. Larson, C. J. Carey, Í. Polat, Y. Feng, E. W. Moore, J. VanderPlas, D. Laxalde, J. Perktold, R. Cimrman, I. Henriksen, E. A. Quintero, C. R. Harris, A. M. Archibald, A. H. Ribeiro, F. Pedregosa, P. van Mulbregt, and SciPy 1.0 Contributors, "SciPy 1.0: Fundamental Algorithms for Scientific Computing in Python," *Nature Methods*, vol. 17, pp. 261–272, 2020.
- [16] J. Newman, "Wave effects on deformable bodies," *Applied Ocean Research*, vol. 16, no. 1, pp. 47–59, Jan. 1994.
- [17] M. Ancellin and F. Dias, "Capytaine: a Python-based linear potential flow solver," *Journal of Open Source Software*, vol. 4, no. 36, p. 1341, apr 2019. [Online]. Available: <https://doi.org/10.21105%2Fjoss.01341>
- [18] A. Babarit and G. Delhommeau, "Theoretical and numerical aspects of the open source BEM solver NEMOH," in *Proceedings of the 11th European Wave and Tidal Energy Conference (EWTEC2015)*, Nantes, France, 2015.

- [19] A. Dallman and V. Neary, *Characterization of U.S. Wave Energy Converter (WEC) Test Sites: A Catalogue of Met-Ocean Data*, 01 2014.
- [20] J. van Rij, Y.-H. Yu, B. Boren, J. Weber, and A. Cardinal, "Internal report on numerical system model implementation: Models are fit for purpose, & internal report on system simulation results," U.S. Patent 0 019 498, Jan. 2010.
- [21] M. Kochenderfer and T. Wheeler, *Algorithms for Optimization*. Cambridge, Massachusetts: The MIT Press, 2019.